Landslides (2018) 15:967–983
DOI 10.1007/s10346-018-0960-x
Received: 30 October 2017
Accepted: 30 January 2018
Published online: 19 February 2018

Xuanmei Fan · Gianvito Scaringi · Qiang Xu · Weiwei Zhan · Lanxin Dai · Yusheng Li · Xiangjun Pei · Qin Yang · Runqiu Huang

Coseismic landslides triggered by the 8th August 2017 M_s 7.0 Jiuzhaigou earthquake (Sichuan, China): factors controlling their spatial distribution and implications for the seismogenic blind fault identification

Abstract On 8th August 2017, a magnitude M_s 7.0 earthquake struck the County of Jiuzhaigou, in Sichuan Province, China. It was the third $M_s \geq 7.0$ earthquake in the Longmenshan area in the last decade, after the 2008 M_s 8.0 Wenchuan earthquake and the 2013 M_s 7.0 Lushan earthquake. The event did not produce any evident surface rupture but triggered significant mass wasting. Based on a large set of pre- and post-earthquake high-resolution satellite images (SPOT-5, Gaofen-1 and Gaofen-2) as well as on 0.2-m-resolution UAV photographs, a polygon-based interpretation of the coseismic landslides was carried out. In total, 1883 landslides were identified, covering an area of 8.11 km², with an estimated total volume in the order of $25–30 \times 10^6$ m³. The total landslide area was lower than that produced by other earthquakes of similar magnitude with strike-slip motion, possibly because of the limited surface rupture. The spatial distribution of the landslides was correlated statistically to a number of seismic, terrain and geological factors, to evaluate the landslide susceptibility at regional scale and to identify the most typical characteristics of the coseismic failures. The landslides, mainly small-scale rockfalls and rock/debris slides, occurred mostly along two NE-SW-oriented valleys near the epicentre. Comparatively, high landslide density was found at locations where the landform evolves from upper, broad valleys to lower, deep-cut gorges. The spatial distribution of the coseismic landslides did not seem correlated to the location of any known active faults. On the contrary, it revealed that a previously-unknown blind fault segment—which is possibly the north-western extension of the Huya fault—is the plausible seismogenic fault. This finding is consistent with what hypothesised on the basis of field observations and ground displacements.

Keywords Coseismic landslides · Jiuzhaigou earthquake · Seismogenic fault · Landslide inventory · Landslide spatial distribution

Introduction

At 21:19:46 local time (13:19:46 UTC) on 8th August2017, a M_s 7.0 earthquake (CENC 2017), M_w 6.5 (USGS 2017), hit the north of Sichuan Province, China, with epicentre in the town of Zhangzha (33.20° N, 103.82° E), Jiuzhaigou County, Aba Prefecture. The seismic shaking lasted for about 15 s (CSI 2017) and was felt in a vast portion of Sichuan Province, including the City of Chengdu, about 285 km away from the epicentre, and in several other provinces. Within the next 36 h, more than 1700 aftershocks were recorded, 30 of which with $M_s \geq 3.0$, with the strongest one being a 4.8 M_s shake at 02:17:04 UTC on 9th August. The Jiuzhaigou County is a popular tourist destination in China, featuring a UNESCO World Heritage Site and a World Biosphere Reserve (UNESCO 1992). More than 175,000 among tourists and locals were affected by the event. More than 73,000 buildings were damaged, 76 of which collapsed. Twenty-five fatalities, 6 people missing and 525 injured were reported until 13th August, 12:00:00 UTC.

The epicentre and focal mechanism of the Jiuzhaigou earthquake did not seem correlated sufficiently with any of the already-known active faults in the area. The seismogenic fault of the Jiuzhaigou earthquake was firstly hypothesised by Li et al. (2017) to be an unknown blind strike-slip fault, on the basis of the combination of the fault mechanism solutions, field-inferred signs of rupture and radon anomalies. However, since the inferred fault slip was rather slight (in the order of a few centimetres: see CSI 2017), the location of the Jiuzhaigou earthquake's seismogenic fault has been debated.

Non-obvious surface ruptures are actually common in moderate to large earthquakes with magnitude $6 \leq M_w \leq 7$ (e.g. Sekiguchi et al. 2000; Semmane et al. 2005; Wei et al. 2011; Xu et al. 2015; Le Béon et al. 2017; Huang et al. 2017) characterised by strike-slip motion. Various geophysical and geomorphological methods have been proposed for the identification and characterisation of blind seismogenic faults (e.g. Hartvich and Valenta 2013; Choi et al. 2015; Bonini et al. 2016; Huang et al. 2017). The peak ground acceleration, the earthquake magnitude, the direction of the seismic waves and the distance from the seismogenic fault are obviously correlated with the distribution pattern of the coseismic landslides (Meunier et al. 2007; Chigira et al. 2010; Qi et al. 2010; Xu et al. 2013a, b, c, d; Odin et al. 2017). Thus, an accurate mapping and analysis of their distribution—besides being fundamental for a reliable assessment of the coseismic and the secondary geohazards, crucial for establishing risk mitigation countermeasures—can be helpful in the identification of the seismogenic fault, also when the surface rupture is not evident (Meunier et al. 2013; Xu and Xu 2014; Zhou et al. 2016).

Within this framework, this work is aimed at providing a detailed landslide inventory, and at delivering a quick statistical assessment of the spatial distribution and controlling factors of the geohazards triggered by the Jiuzhaigou earthquake, with the two-fold scope of providing a first tool for the risk assessment related to possible secondary geohazards, and of supporting the seismogenic fault identification for further seismic hazard assessments.

Study area

The area object of this study extends for about 840 km² around the earthquake's epicentre in Zhangzha Town, near the northern

boundary of Sichuan Province. It is located in the northern part of the Minshan mountain range, in the transition zone from the Qinghai-Tibet Plateau to the Sichuan Basin, and it is crossed by the Bai River, the Jiuzhai gully and the Rizhai gully. The area features deep-incised valleys shaped by glacial, hydrological and tectonic activity. The average elevation is over 4000 m a.s.l, with peaks over 4700 m a.s.l., a minimum of 1160 m a.s.l. in the river valley and slope gradients generally higher than 30°.

The Jiuzhaigou area lies in the Songpan-Ganzi sub-block in the east of the Bayan Har block, in the middle section of the well-known North-South seismic zone in China, where the recurrence time of earthquakes with magnitude larger than 7.0 can be as low as 14.2 years (Ren et al. 2002). The eastward extrusion of the Songpan-Ganzi sub-block, which obliquely collides with the western Qinling fold belt and the Longmenshan thrust belt, results in five known main faults in the Songpan-Ganzi tectonic boundary (Fig. 1), i.e. the Wenxian-Maqin (1), Minjiang (2), Huya (3), Qingchuan-Pingwu (4) and Xueshan (5) faults. These seismogenic structures all have a potential for earthquakes of magnitude $M_L \geq 7.5$ (Li et al. 2016a). The northern boundary of the Songpan-Ganzi block (the Wenxian-Maqin fault) protrudes sharply southward, while the south boundary fault (the Qingchuan-Pingwu fault) protrudes northward slightly, forming a tectonic bottleneck zone in the Songpan-Jiuzhaigou area. The eastward extrusion of the Songpan-Ganzi block is locked, and this causes a high crustal stress concentration in this zone.

Xu et al. (2008) showed that the Bayan Har block is cut into two sub-blocks by the Longriba fault, namely the Aba sub-block in the west and the Longmenshan sub-block in the east. The translational velocity of the Aba sub-block is about 11.4 mm/year eastward, while that of the Longmenshan sub-block is about 8.5 mm/year in N116° E direction (Lu et al. 2003; Shen et al. 2005). The difference of velocity is absorbed by the right-lateral faulting and thrusting in the adjacent areas (Xu et al. 2008). The left-lateral strike-slip rate of the Wenxian–Maqin fault since the late Cenozoic is ~ 9.7 mm/year, while the right-lateral strike-slip rate of the Qingchuan-Pingwu fault is ~ 5.1 mm/year (Li et al. 2017). The Minjiang fault is dominated by thrusting, with vertical slip rates of 0.4–0.5 mm/year, while the Huya fault is dominated by left-lateral strike slip, with horizontal slip rates of about 1.4 mm/year (Zhou et al. 2006).

The Jiuzhaigou area suffered more than 50 events with $M_s \geq 5$ in the past century, some of which with $M_s \geq 7$ (CENC 2017). The epicentre of the 8th August 2017 event is located just 65 km to the east of the epicentre of the M_s 8.0 Wenxian earthquake that struck the Wenxian-Maqin fault in 1879 (Li et al. 2017), 65 km to the northwest of the epicentre of the 1976 M_s 7.2 Songpan-Pingwu earthquake that struck the Huya fault (Chen et al. 1994), about 130 km to the north of the epicentre of the 1933 M_s 7.5 Diexi earthquake that possibly struck the Minjiang fault (Chen et al. 1994) or the Sonpinggou fault (Ren et al. 2017), and about 245 km to the north of the epicentre of the 2008 M_s 8.0 Wenchuan earthquake that struck the Yinxiu-Beichuan fault (Dai et al. 2011; Huang et al. 2012).

The regional geology of the epicentral area features outcrops of the Middle to Late Triassic sedimentation (see Fig. 2). The area is characterised by a thick sequence of Triassic strata of deep marine deposits, commonly referred to as the Songpan-Ganzi flysch complex, which was intensely deformed by folding and thrusting during the Late Triassic and Early Jurassic (Yin and Harrison 2000).

Data and methods

To quantify and analyse the coseismic geohazards statistically, a landslide inventory was compiled through the interpretation and cross-checking of high-resolution images from different sources (Table 1; Fig. 3) over a study area of 840 km^2. Satellite images from Spot-5 with 2.5 m resolution were used as the pre-earthquake data, while the Chinese Gaofen-1 and Gaofen-2 satellites were the source of 1 m resolution images taken soon after the earthquake. Some very high-resolution (0.2 m) aerial images of key areas were also acquired within 72 h after the earthquake through UAV photography (Table 1; Fig. 3). The images were adjusted through geometric correction, colour enhancement and coordinate system conversion to facilitate their interpretation.

The study area is mostly covered by dense vegetation. Thus, the use of automatic tools for the identification of coseismic landslides and discrimination from pre-existing landslides was deemed unfeasible, and a more time-consuming polygon-based visual interpretation in GIS environment with in situ checks was performed to ensure the high-quality of the landslide mapping. The landslide classification was chosen in compliance with the updated classification by Hungr et al. (2014). Some examples of coseismic landslides identified by comparing pre- and post-earthquake images are shown in Fig. 4. As part of the relevant information for the analysis of the controlling factors and susceptibility derives from the sole source areas, the latter were mapped separately from the deposition areas. For a few hardly identifiable cases, the uppermost 35% of the landslide area was assumed to be the source area, on the basis of empirical relationships (Corominas 1996) between landslide size, slope angle and runout distance.

Terrain data, geological data and earthquake data were also acquired, so that the analysis of the main controlling factors of the coseismic landslides could be performed, and hence a quick evaluation of the landslide susceptibility in the area (Table 1) and the identification of the most typical landslide characteristics could be carried out. The 5 m resolution pre-earthquake DEM, provided by the Sichuan Bureau of Surveying and Mapping, was used to produce the map containing the topographic attributes (slope angle, aspect, elevation etc.). The geological map with scale 1:200,000 was acquired from the Sichuan Bureau of Geological Exploration and Exploitation of Mineral Resources. The seismic data were obtained from the China Earthquake Networks Center (CENC 2017).

The spatial distribution analysis was performed in GIS environment through spatial statistical analysis functions. Eight factors were considered for the statistical analysis, namely the Peak Ground Acceleration (PGA), the distance from the hypothesised seismogenic fault, the elevation, the slope gradient, the slope aspect, the lithology and the distance from rivers and from roads. The raster layers of different factors were prepared and classified, and the relative occurrence probability of the different classes for each factor were calculated. A binary logistic regression model (e.g. Schumacher et al. 1996; Menard 2002; Mathew et al. 2009) was adopted to evaluate the geohazard susceptibility. As there is no specific requirement on the statistical distribution of the factors

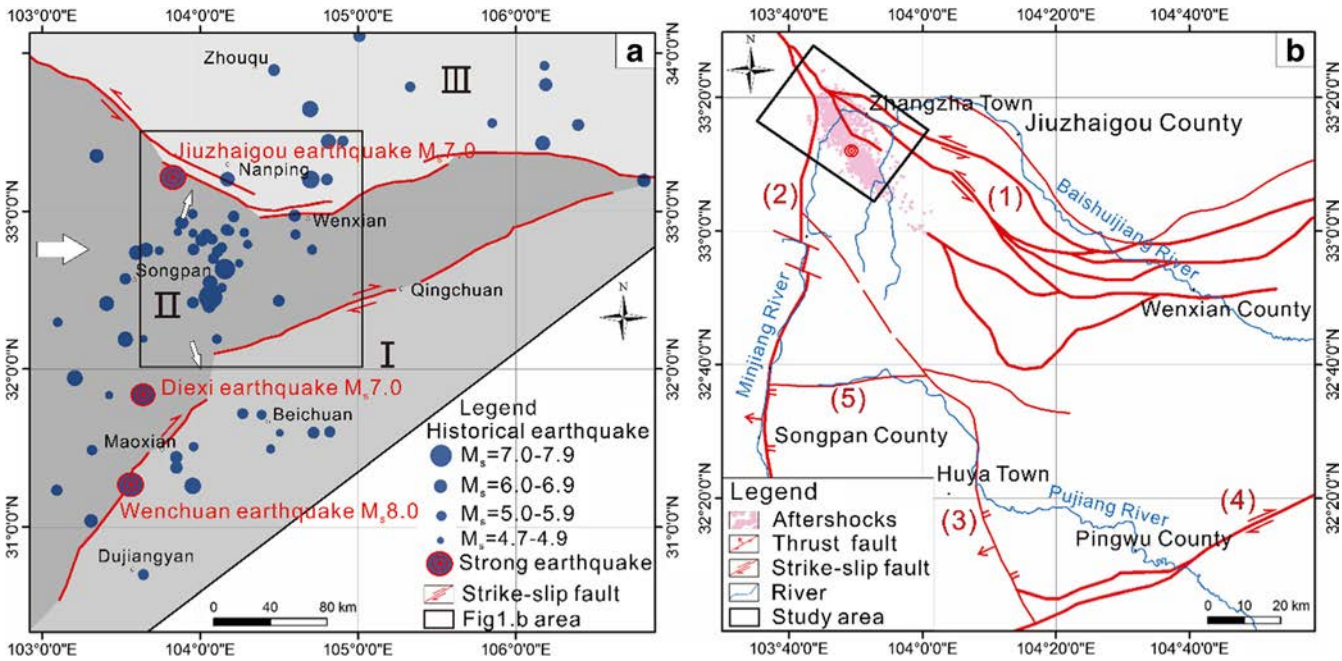

Fig. 1 Location of the 2017 Jiuzhaigou earthquake and tectonic setting of the study area: **a** Longmenshan thrust belt (I), Songpan-Ganzi block (II) and Western Qinling fault block (III); **b** Wenxian-Maqin fault (1), Minjiang fault (2), Huya fault (3), Qingchuan-Pingwu fault (4) and Xueshan fault (5)

(Dai et al. 2002; Dai and Lee 2003), a binomial distribution was assumed under the hypothesis of independence of the controlling factors. Further details on the susceptibility assessment are given in the electronic supplementary material (Online resource 1).

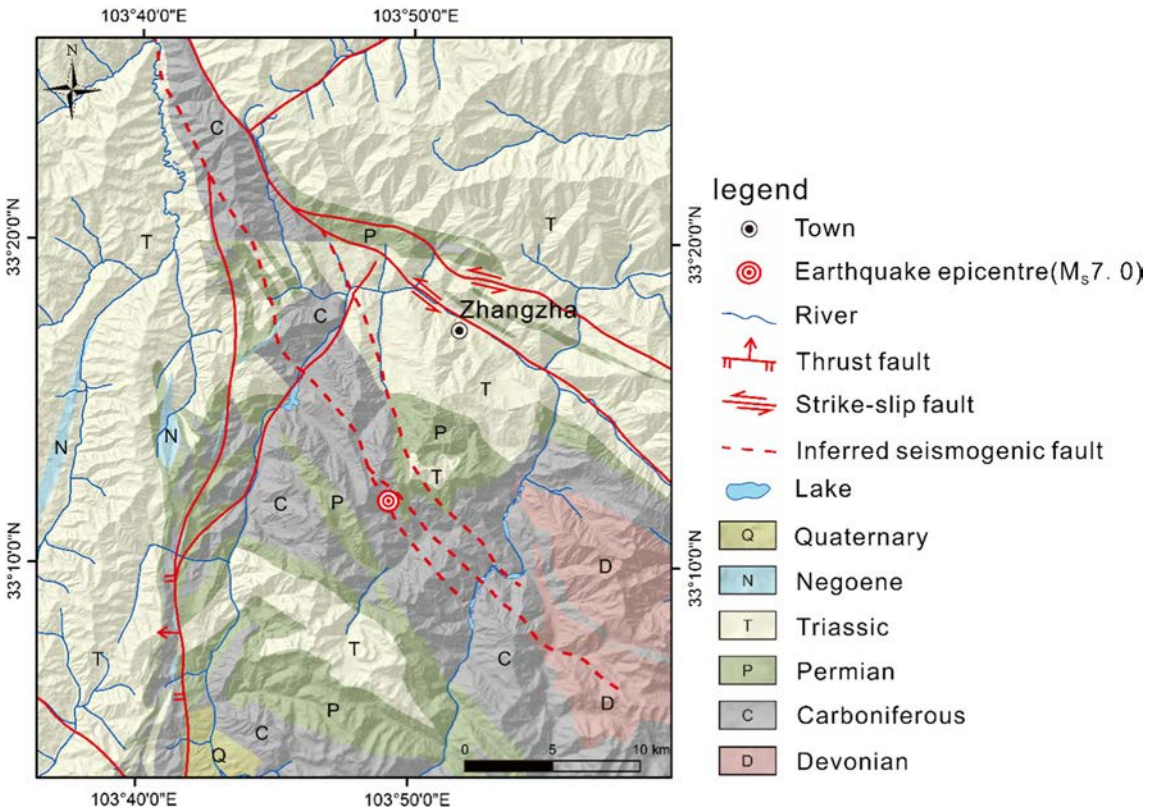

Fig. 2 Geological map showing the outcropping formations, the major faults and the field-inferred (Li et al. 2017) slight surface ruptures caused by the seismogenic fault in the Jiuzhaigou area

Table 1 Remote sensing images and other geographical information data

Data type	Source	Date	Resolution
Image	Spot-5	21 Dec 2015	2.5 m
	Spot-5	7 Dec 2015	2.5 m
	UAV aerial image	11 Aug 2017	0.2 m
	Gaofen-2	9 Aug 2017	1 m
	Gaofen-1	16 Aug 2017	1 m
Terrain model (DEM)	Sichuan Bureau of Surveying, Mapping and Geoinformation	Pre-earthquake	5 m
Geological map (scale, 1:200,000)	Sichuan Bureau of Geological Exploration and Exploitation of Mineral Resources	Pre-earthquake	–
Earthquake	China Earthquake Networks Center	9 Aug 2017	–

Spatial distribution patterns of the coseismic landslides and controlling factors

In total, 1883 landslides were identified (Fig. 5). Some typical, representative examples, are shown in Fig. 6: like most of the coseismic landslides triggered by the Jiuzhaigou earthquake, they are small-scale shallow rock/debris slides and rockfalls (Hungr et al. 2014 classification) that occurred in the lower part of rather steep slopes (35–55°), in proximity of the road network, that crosses the valleys in the epicentral area with frequent inslope sections constructed with seemingly insufficiently reinforced slope cuts. Details of the typical landslide characteristics based on the controlling factor analysis are given in the next sub-sections.

The largest landslide covers about 231,000 m^2 in horizontal projection, while the smallest one is just 9.7 m^2. The average area is about 4307 m^2, and the total landslide area is 8.11 km^2. The total landslide volume was estimated to be in the order of 15–85 × 10^6 m^3

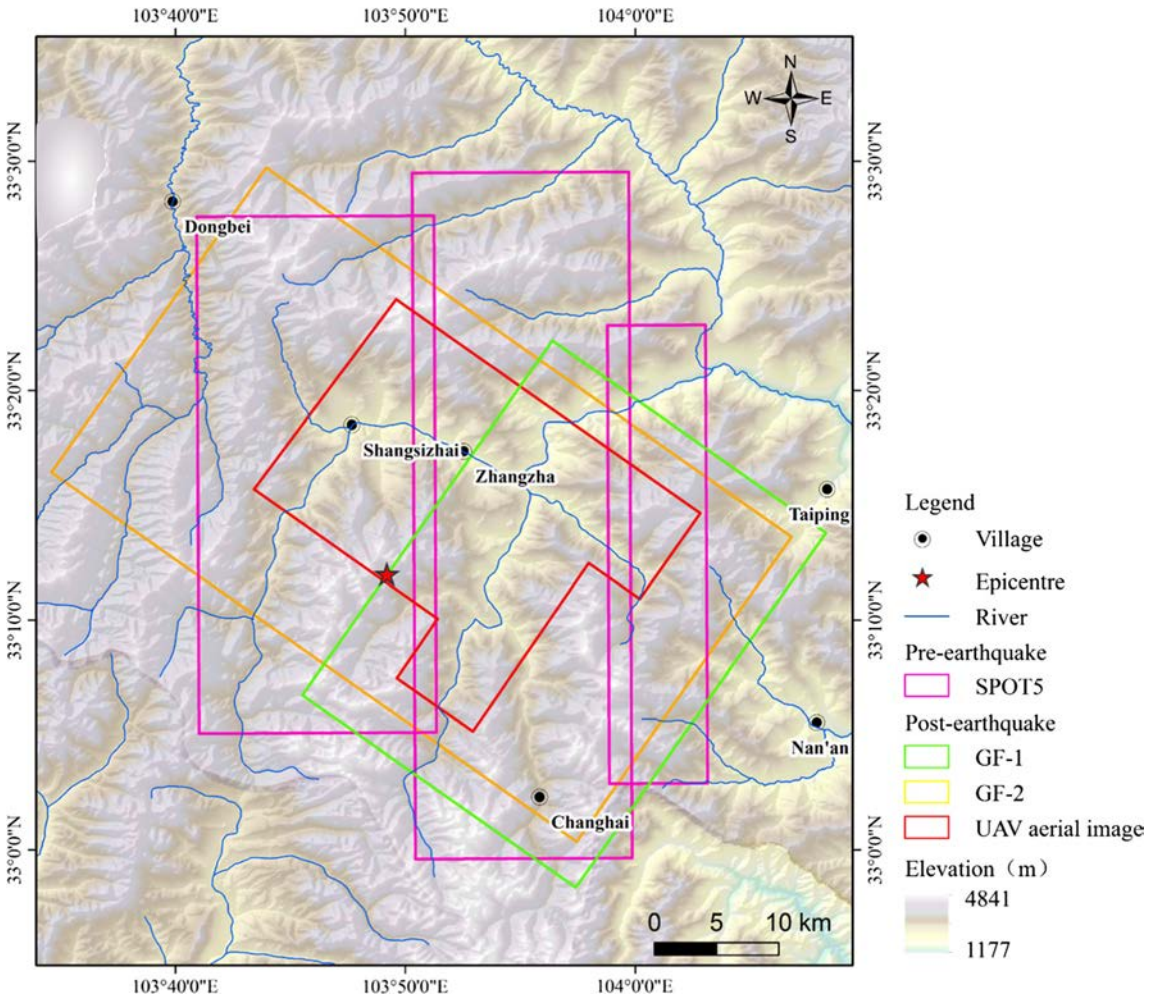

Fig. 3 Pre- and post-earthquake remote sensing imagery coverage map

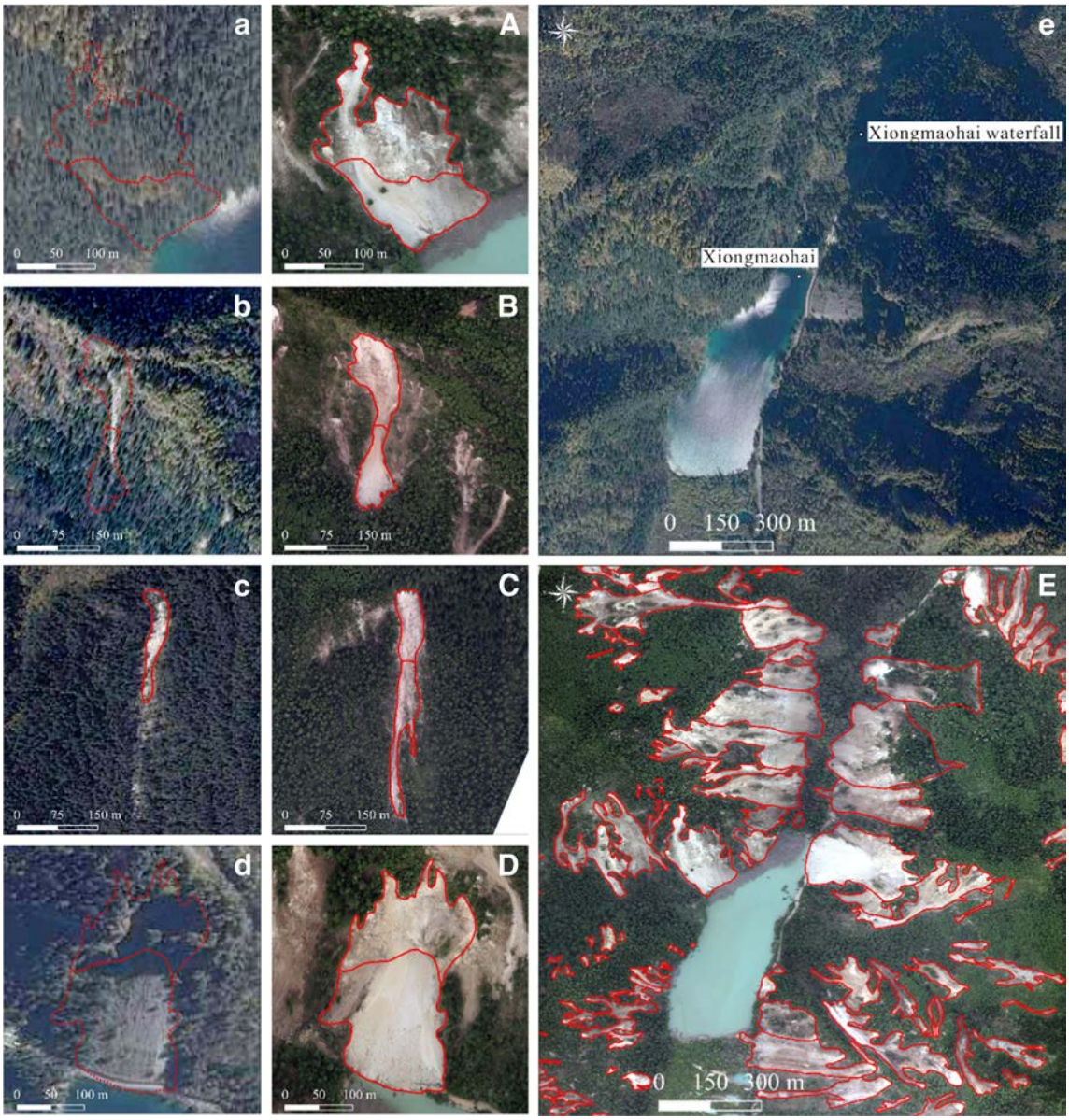

Fig. 4 Examples of coseismic landslide interpretation based on high resolution pre-earthquake (a–e) and post-earthquake (A–E) images

on the basis of various area-volume empirical relationships (Guzzetti et al. 2009; Larsen et al. 2010; Parker et al. 2011; Xu et al. 2016), which were calibrated by the respective authors on different datasets of field measurements and remote sensing images of landslides of different types and different sizes. The range of volume (V) = 25–30 × 10^6 m^3, obtained using the equation proposed by Larsen et al. (2010) and the associated uncertainty (± 1 standard deviation), was considered to be the most reliable, given the large size of the dataset used by the authors for calibration, and considering that such dataset comprises both soil and bedrock landslides, also of very small size. On the contrary, for instance, the equation proposed by Xu et al. (2016) was discarded as it was calibrated on landslides with $A > 10{,}000$ m^2 only. Details on the equations, on the related uncertainties and on the reliability for the application to the present case, are given in detail in the electronic supplementary material (Online resource 2).

The inventory map (Fig. 5) shows that the coseismic landslides are not clustered evenly around the epicentre. Instead, they are mostly located at Jiudaoguai, i.e. at the junction between the field-inferred blind fault (F1 in Fig. 5) and the secondary fault of Minjiang fault and at Xiongmaohai, i.e. at the SE end of the field-inferred blind fault. The areas also correspond to two NE-SW oriented valleys, which are typical deep-cut valleys shaped by Quaternary glacial activity and feature several historical marine lakes (Fig. 5).

The spatial distribution of the coseismic landslides can be correlated with seismic, terrain and geologic factors (Keefer 2000, 2002; Huang and Li 2008; Xu and Li 2010a, b; Xu et al. 2013a, b, c, d; Xu and Xu 2013; Fan et al. 2017). To identify the most relevant factors controlling the Jiuzhaigou coseismic landslides, eight factors belonging to these three categories (terrain, geology, seismology) were considered. Each attribute map was divided into

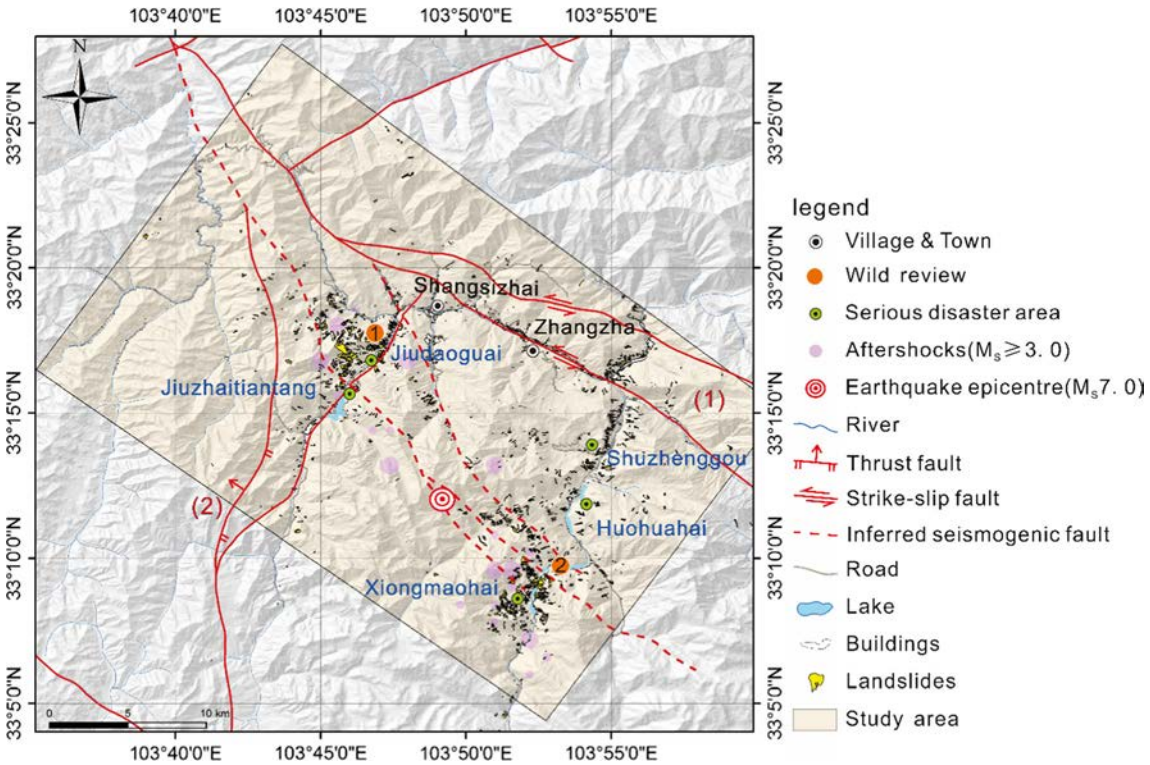

Fig. 5 Distribution of landslides triggered by the Jiuzhaigou earthquake with indication of faults, aftershocks and tourist attractions. The "wild reviews" indicate the locations of the landslides shown in Fig. 6

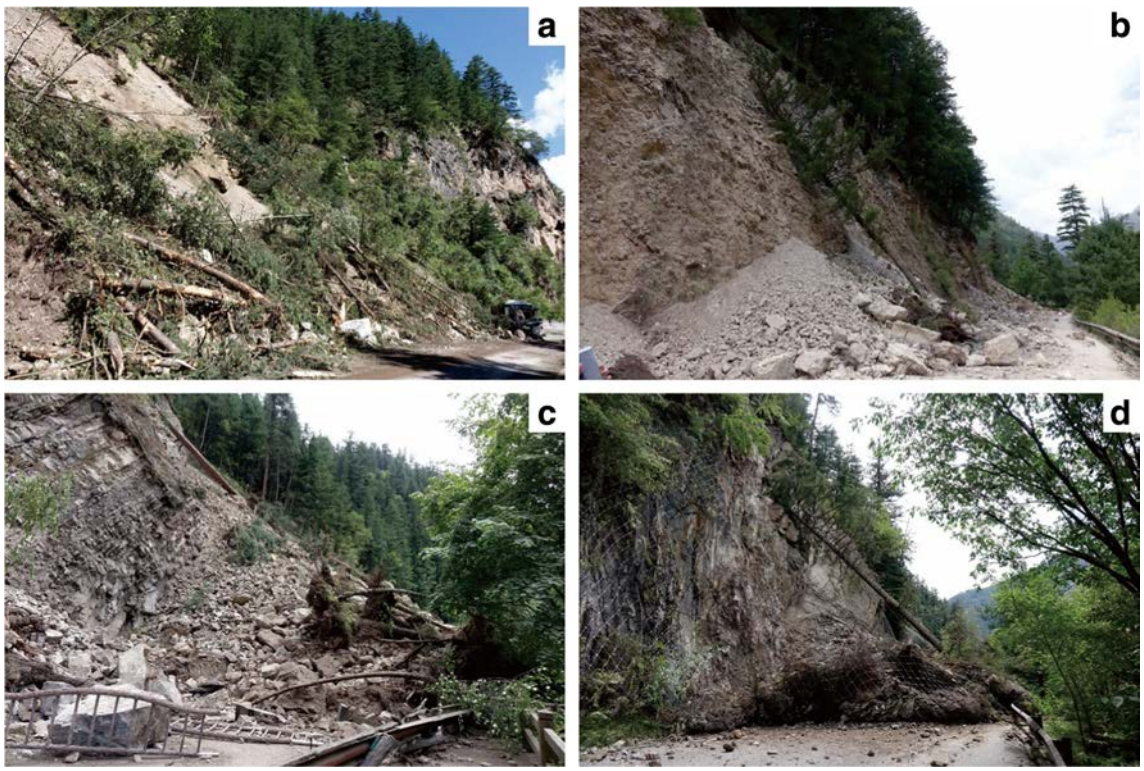

Fig. 6 Typical landslides revealed by the field investigation: **a** debris slide (location: wild review 1 in Fig. 5) and **b** rock fall, **c** rock slide and **d** rock topple (location: wild review 2 in Fig. 5)

discrete classes (Table 2). Then, through spatial statistics tools in GIS environment, the number and the cumulated area of the landslides falling in each class of each attribute were calculated. The "landslide number density" was defined as the number of coseismic landslides in 1 km^2, and the "landslide areal density" was defined as the ratio between the area covered by the coseismic landslides and the total area of the class.

Seismic factors

The tectonic setting of the Jiuzhaigou earthquake area is complex (see the "Study area" section). Even though the focal mechanism solution and the aftershock distribution both indicate that its causative fault movement was dominated by a NW-SE-oriented left-lateral strike-slip (CENC 2017; Li et al. 2017), the identification of the seismogenic fault is not obvious as there is no clear surface rupture. Li et al. (2017) identified two possible slight surface ruptures with length of 23.0 and 19.0 km, respectively, with relative displacement of just 0.015–0.035 m, which they believed to be the surface ruptures of the seismogenic fault and of its secondary fault. Their hypothesis was supported by abnormal radon measurements along these ruptures. Nevertheless, there are controversies in the seismogenic fault identification, as the Tazang fault, the central part of the Wenxian-Maqin fault and the Huya fault are also NW-SE oriented and located relatively close to the Jiuzhaigou earthquake epicentre (see Fig. 2).

The seismogenic fault can exert a strong control on the coseismic landslide distribution, as observed in several earthquakes (Keefer 1984, 2000; Sato et al. 2007; Huang and Li 2009; Gorum et al. 2011; Xu et al. 2013b). Thus, a statistical analysis was used to infer the seismogenic fault based on the landslide distribution. In GIS environment, buffer areas with 1 km distance intervals from the candidate faults were first generated. Then, the landslide areal density in each buffer area was calculated and the relationship between the landslide areal density and the distance from the candidate seismogenic fault was analysed. As shown by Fig. 7b (bottom), most of the landslides (total area = 5.3 km^2, i.e. ~ 65% of the total landslide area) occurred within 2 km from the field-inferred (Li et al. 2017) blind fault (F1 in Fig. 2), particularly in the NE plate (the active plate), and the highest landslide area, areal density and number density were evaluated within 1 km from the fault. Coseismic landslides were not found more than 7 km away from the fault. Conversely, by hypothesising the Wenxian-Maqin fault as the causative fault, the landslide area, areal density and number density would increase with the distance from the fault and peak 9 km away (Fig. 7b, top), which seems unreasonable. For comparison, the M_s 8.0 Wenchuan earthquake produced landslide clusters within just 5 km distance from the northern portion of the seismogenic fault, which was dominated by strike-slip motion (Gorum et al. 2011). It seems reasonable that the blind-rupture of the comparatively weaker M_s 7.0 Jiuzhaigou earthquake was unlikely to result in a wider zone affected by landslides, and the field-inferred blind fault can thus be considered the most likely seismogenic fault. This fault possibly constitutes the north-western extension of the Huya fault (see Fig. 1). The distribution of landslides with the distance from the blind fault F1 is given also in Fig. 8a for comparison with other controlling factors.

The main-shock PGA in the study area was between 0.08 and 0.26 g. As shown by Fig. 8b, the landslide area is comparatively higher in PGA 0.2 g class and in 0.24 g class, which account for 73% of the total landslide area. The landslide areal density increases sharply for PGA ≥ 0.18 g and peaks with a value of 1.39% in the 0.26-g PGA class.

Terrain factors

A contour map with 200 m elevation intervals was generated and analysed. Nearly 61% of all landslides clustered between 2600 and 3200 m a.s.l., although this area only accounts for 30% of the total study area (Fig. 8c). The peak landslide areal density, 1.4%, was evaluated at elevations from 2800 to 3000 m a.s.l. The areal density below 2200 m a.s.l. is higher than that above 3200 m a.s.l. (0.82 and 0.13%, respectively), possibly because of the concentration of coseismic landslides along roads and rivers and also because of possibly incomplete remote-sensing interpretation in the high-elevation areas covered by snow.

Landslide inventories of nearby earthquakes showed that most of the landslides triggered by the Wenchuan earthquake occurred along slopes with inclination between 20° and 50° (Huang and Li 2008), and most of the landslides triggered by the Lushan earthquake occurred along slopes with inclination of 30–50° (Chang et al. 2016). For comparison, most of the landslides triggered by the 2017 Jiuzhaigou earthquake occurred on slopes with inclination of 35–55° (Fig. 8d).

The relationships between landslide distribution and the distance to roads and rivers are shown in Fig. 8e, f. The landslide area and areal density decrease with the distance in similar way for both factors, because most of the road network in the study area was built in close proximity to the river network. Relative larger values are found within 1 km from the rivers or roads, with 58% of the total landslides occurring in this area. The landslide abundance along the road network points out a possible, important anthropic influence on landslides occurrence, which deserves further investigation and suggests that the number of coseismic landslides might be greatly reduced through preventive slope reinforcement works along the roadways.

The coseismic mass wasting affected different portions of the slopes unevenly. To visualise the distribution of the coseismic landslides comprehensively, their area, number density and relative position with respect to the top and to the bottom of the slope were plotted on a virtual slope profile (Fig. 9). In the diagram, the horizontal axis is the relative distance of the landslide boundary to the top of the slope (the mountain ridge), while the vertical axis is the relative distance to the bottom of the slope (the river valley). The marker size is consistent with the landslide area. The relative landslide density is displayed by different background colours, with the red colour indicating high density and the blue colour indicating low density. A marker close to the origin of the axes indicates a landslide which covers a large proportion of the slope. Conversely, a small shallow failure is indicated by a small marker close to the surface of the virtual slope. The representation in Fig. 9 allows for the following observations: most of the small-scale landslides (with area up to 1000 m^2) occurred in the lower section of the slope (relative distance to the valley less than 0.5) or very close to the ridge (relative distance to the top less than 0.1); most of the comparatively larger landslides (with area > 1000 m^2) involved the middle part of the slope; several tens of landslides

Table 2 Classification of the seismic, terrain and geologic controlling factors used in the spatial distribution analysis

Factor type	No.	Factor	Classification
Seismic	1	Peak ground acceleration (PGA) (g)	(1) < 0.08; (2) 0.08 ~ 0.10; (3) 0.10 ~ 0.12; (4) 0.12 ~ 0.14; (5) 0.14 ~ 0.16; (6) 0.16 ~ 0.18; (7) 0.18 ~ 0.20; (8) 0.20 ~ 0.22; (9) 0.22 ~ 0.24; (10) 0.24 ~ 0.26.
	2	Distance to seismogenic fault (km)	(1) < 1; (2) 1 ~ 2; (3) 2 ~ 3; (4) 3 ~ 4; (5) 4 ~ 5; (6) 5 ~ 6; (7) 6 ~ 7; (8) 7 ~ 8; (9) 8 ~ 9; (10) 9 ~ 10; (11) 10 ~ 11; (12) 11 ~ 12; (13) 12 ~ 13; (14) 13 ~ 14; (15) 14 ~ 15; (16) > 15.
Terrain	3	Elevation (m)	(1) < 2200; (2) 2200 ~ 2400; (3) 2400 ~ 2600; (4) 2600 ~ 2800; (5) 2800 ~ 3000; (6) 3000 ~ 3200; (7) 3200 ~ 3400; (8) 3400 ~ 3600; (9) 3600 ~ 3800; (10) 3800 ~ 4000; (11) 4000 ~ 4200; (11) > 4200.
	4	Slope angle (deg)	(1) < 10; (2) 10 ~ 20; (3) 20 ~ 30; (4) 30 ~ 35; (5) 35 ~ 40; (6) 40 ~ 45; (7) 45 ~ 50; (8) 50 ~ 55; (9) 55 ~ 60; (10) > 60.
	5	Slope aspect/fault slip direction	(1) FLAT; (2) N; (3) NE; (4) E; (5) SE; (6) S; (7) SW; (8) W; (9) NW.
	6	Distance to rivers (m)	(1) 0 ~ 500; (2) 500 ~ 1000; (3) 1000 ~ 1500; (4) 1500 ~ 2000; (5) 2000 ~ 2500; (6) 2500 ~ 3000; (7) 3000 ~ 3500; (8) 3500 ~ 4000; (9) 4000 ~ 5000; (10) 5000 ~ 6000
	7	Distance to roads (m)	(1) 0 ~ 500; (2) 500 ~ 1000; (3) 1000 ~ 1500; (4) 1500 ~ 2000; (5) 2000 ~ 2500; (6) 2500 ~ 3000; (7) 3000 ~ 3500; (8) 3500 ~ 4000; (9) 4000 ~ 5000; (10) 5000 ~ 6000
Geologic	8	Lithology	(1) N2; (2) T3; (3) T2; (4) T1; (5) P2; (6) P1; (7) C3; (8) C2; (9) C1; (10) D3.

reached the rivers, as shown by the red markers in the bottom of the virtual slope. Fortunately, these landslides did not produce any dammed lakes according to the field investigation, but they can enhance the sediment transport by the rivers (e.g. Li et al. 2016b; Croissant et al. 2017). The comparatively higher density of landslides in the lower portion of the slopes might be due to the micro-landform observed in the study area. In fact, the slopes in the Jiuzhaigou area are characterised by wider valleys with relatively gentle slopes at high elevation and by a rather sharp transition into gorges with steep scarps due to strong gully erosion (Fig. 10).

In order to investigate the correlation between the direction of movement of the blind strike-slip fault and the slope aspect, the landslide area, areal density and number density were subdivided in classes according to the angle difference Δ° between the slope aspect and the direction of movement of the NE plate (331°). The results of the analysis are shown in Fig. 8g. Slopes whose aspect is

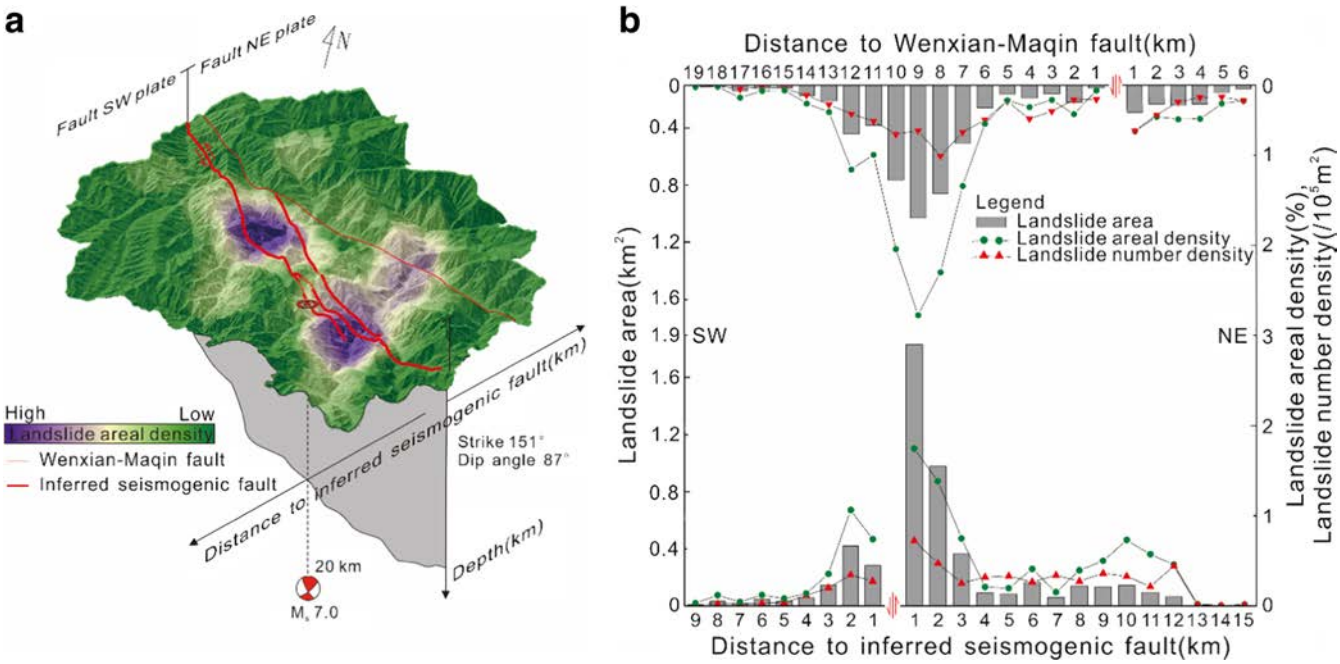

Fig. 7 Relationship between the landslide areal density and two potential seismogenic faults of the Jiuzhaigou earthquake: **a** view of the study area with indication of the landslide areal density and location of the faults; **b** relationship between landslide area, areal density and number density and the distance from the field-inferred seismogenic fault (blind fault F1 in Fig. 5, bottom) and from the Wenxian-Maqin fault (top)

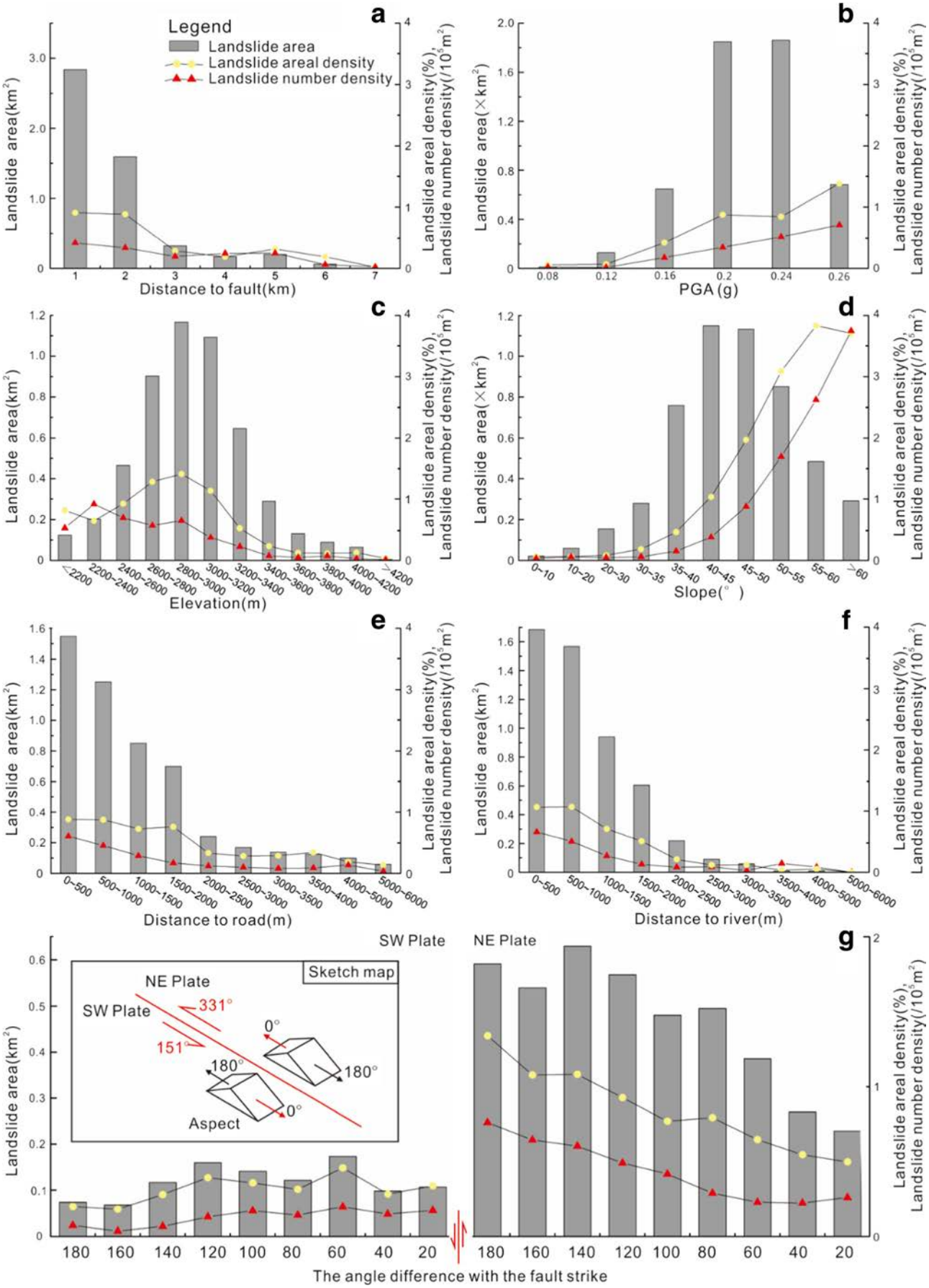
a
Legend
Landslide area
Landslide areal density
Landslide number density
Landslide area(km²)
Landslide areal density(%),
Landslide number density(/10⁵m²)
Distance to fault(km)
b
Landslide area(×km²)
PGA (g)
c
Elevation(m)
d
Slope(°)
e
Distance to road(m)
f
Distance to river(m)
g
SW Plate
NE Plate
Sketch map
331°
151°
0°
180°
Aspect
The angle difference with the fault strike

Fig. 8 Possible controlling factors for the coseismic landslides triggered by the Jiuzhaigou earthquake: **a** distance from the seismogenic fault, **b** PGA, **c** elevation, **d** slope angle, **e** distance to road and **f** distance to river. In (**g**), the relationship between slope aspect and fault orientation is analysed: on the left side, landslides on the NE plate are reported, where the fault slip direction was 331°; on the right side, landslides on the SW plate are reported, where fault slip direction was 151°

parallel and concordant with the movement direction of the NE plate (331°) have Δ° = 0. Conversely, slopes whose aspect is parallel and discordant with the movement direction of the NE plate, i.e. the aspect is concordant with the movement direction of SE plate, have Δ° = 180° (Fig. 8g). High values of landslide area, areal density and number density are found on slopes with high Δ° on the NE plate and on slopes with low Δ° on the SW plate. In other words, the analysis shows that the coseismic landslides are more abundant along slopes in which the movement of the plate acted as a destabilising force. Furthermore, landslides are much more abundant on the NE plate (active plate) than on the SW plate (passive plate). A similar correlation between the direction of movement of the fault and the slope aspect was observed by Xu et al. (2013b) for the M_s 7.1 strike-slip Yushu earthquake, which was characterised by similar seismic intensity and fault geometry.

Geological factors

According to the geological map provided by the Sichuan Bureau of Geological Exploration and Exploitation of Mineral Resources (scale 1:200,000), ten geological formation units outcrop in the study area (Fig. 2). The coseismic landslide distribution with respect to the outcropping formations are presented in Fig. 11. Most of the coseismic landslides (5.85 km^2) occurred in Mesozoic Formations that mainly consists of limestone, accounting for 72.1% of the total landslide area, while the total area of the Mesozoic Formations outcrops only constitutes 31.1% of the total study area. The Carboniferous Formations exhibits the largest landslide areal density (1.67%), followed by the Permian Formations. On the other hand, the Neogene Formation, which consists of conglomerate and sandy gravel, appears to be the least susceptible zone landslides, possibly simply because of its distance from the seismogenic fault, low PGA and low slope steepness (see Figs. 2 and 5).

Discussion

Strong continental earthquakes can induce massive geohazards, causing severe economic loss and a large number of casualties. The 2008 M_s 8.0 Wenchuan earthquake triggered nearly 200,000 landslides, more than 60,000 of which with an area larger than 35,000 m^2 (Huang and Li 2009; Gorum et al. 2011; Huang and Fan 2013; Xu et al. 2013a). It produced more than 800 dammed lakes (Fan et al. 2012, 2015, 2017) and sharply increased the debris flow activity, which will likely take decades to normalise (e.g. Zhang and Zhang 2017). The death toll of the chain of geohazards has been evaluated in one third of the total number of casualties caused by the earthquake (e.g. Wang et al. 2014). Relatively weaker earthquakes can cause serious hazards as well. In 2013, the M_s 7.0 Lushan earthquake triggered 1129 landslides over an area of 2200 km^2 (Chen et al. 2013; Xu et al. 2015; Tang et al. 2015), and the M_L 6.5 Ludian County earthquake in Yunnan Province in 2014 caused more than 1800 landslides (Zhou et al. 2016). Worldwide, a tremendous number of geohazards was triggered in recent times, for instance, by the 1999 M_w 7.5 Chi-Chi earthquake in Taiwan, by the 2004 M_w 6.6 Mid-Niigata Prefecture Earthquake in Japan, by the 2005 M_w 7.6 Kashmir earthquake in Pakistan, by the 2010 M_w 7.0 Haiti earthquake and by the 2015 M_w 7.9 Nepal earthquake (e.g. Keefer 2002; Chigira et al. 2003; Chigira and Yagi 2006; Sato et al. 2007; Gorum et al. 2013; Xu et al. 2014; Kargel et al. 2016; Roback et al. 2017). It is evident that a reliable assessment of the earthquake-induced geohazards and of their secondary geohazards chain is crucial for establishing risk mitigation countermeasures. Indeed, the scientific community is working strenuously, after each event, on the inventory, spatial distribution, mechanism and risk assessment of coseismic geohazards and on the forecasting and prevention of post-seismic geohazards (e.g. Keefer 2010; Qi et al. 2010; Dai et al. 2011; Huang et al. 2012; Has and Nozaki 2014; Xu et al. 2014; Xiaoli et al. 2015; Chen et al. 2017; Fan et al. 2017; Roback et al. 2017; Robinson et al. 2017; Tanoli et al. 2017).

Comparison with other coseismic landslide inventories

In Fig. 12, the total area, total estimated volume and landslide number density resulting from the Jiuzhaigou coseismic landslide inventory are compared with those relative to several earthquakes worldwide (Keefer 1984, 1994; Xu et al. 2015; Marc et al. 2016). Both Keefer (1984) and Xu et al. (2015) identified a linear relationship between the earthquake magnitude and the logarithm of the total landslide area. The points relative to the Jiuzhaigou coseismic landslide inventory fit within this trend, as shown by Fig. 12a, b. Similarly, Marc et al. (2016) hypothesised a linear relationship between the logarithm of the earthquake magnitude and the logarithm of the total estimated landslide volume. The point relative to the Jiuzhaigou earthquake is in good agreement with this empirical relationship (Fig. 12c). However, it can be seen in Fig. 12a that earthquakes with the same magnitude can result in landslide areas which differ by up to 2 orders of magnitude. The Jiuzhaigou earthquakes resulted in a comparatively low landslide area. This might be related to the relatively low PGA (0.26 g) and MMI intensity (VIII, limited to an area of 155.8 km^2). By comparison, the Lushan earthquake, characterised by the same magnitude (M_s = 7.0) as that of the Jiuzhaigou earthquake, triggered landslides with a total area more than ten times greater (Xu et al. 2015).

The 2008 M_s 8.0 Wenchuan earthquake, the 2013 M_s 7.0 Lushan earthquake and the 2017 M_s 7.0 Jiuzhaigou earthquake struck the same region during the last decade but had different fault mechanisms, namely: a combination of thrusting and strike-slip, blind reverse-slip and blind strike-slip respectively (e.g. Xu et al. 2009). They occurred in areas with similar topographic and climatic conditions, and their epicentres seem sufficiently far from each other to exclude that an earlier earthquake could have acted as a predisposing factor in triggering more coseismic landslides during a more recent event. Thus, by comparing the landslide distribution patterns relative to these three events, the influence of the fault mechanism on the landslide distribution can be highlighted. In Fig. 12d, a comparison is done using the three-parameter inverse-gamma distribution proposed by Malamud et al. (2004). The landslide frequency density, f (vertical axis), is defined as the ratio between the landslide number within the corresponding landslide

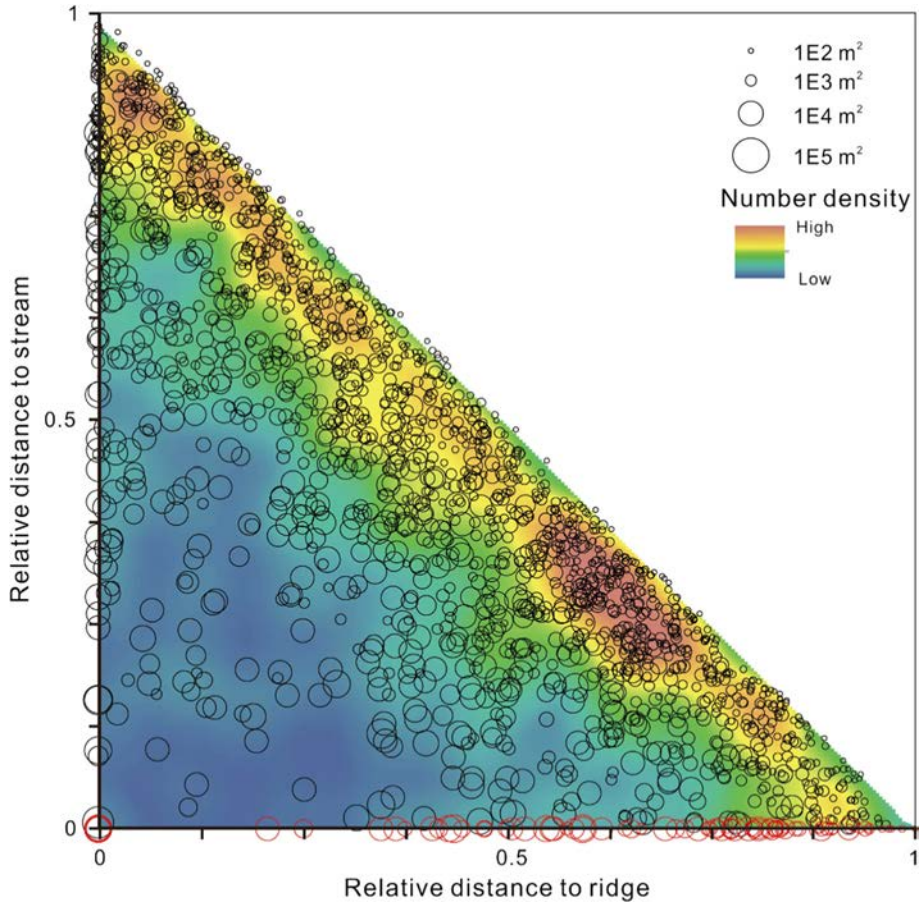

Fig. 9 Virtual slope representation showing the coseismic landslide distribution in different portions of the slope. The horizontal axis is the relative distance of the landslide boundary to the top of the slope (the mountain ridge), while the vertical axis is the relative distance to the bottom of the slope (the river valley). The marker size is proportional to the logarithm of the landslide area. The landslide number density is displayed by different background colours, with red indicating comparatively high density and blue indicating comparatively low density

area class and the total number of landslides in the whole inventory. The rollover point (modal landslide area) divides the curve into two parts, with relatively small landslides on the left side and relatively large landslides on the right. It can be seen that the modal landslide area of the Jiuzhaigou earthquake is two times bigger than that of the Lushan earthquake (despite having the same magnitude), but about seven times smaller than that of the Wenchuan earthquake (300, 150 and 2000 m^2, respectively). The frequency densities of the Jiuzhaigou coseismic landslides are higher than those of the Lushan coseismic landslides for all area classes. The frequency density of small landslides is even higher than that of the Wenchuan earthquake, although this might be an effect of the limited resolution of the landslide inventory of this latter. Conversely, the frequency density of large landslides triggered by the Jiuzhaigou earthquake is 1 to 2 orders of magnitude smaller than that of the Wenchuan earthquake.

Coseismic landslides tend to distribute along the seismogenic fault, but the width of the landslide-affected area depends on the type of faulting and is not symmetric on the two sides of the fault. For the Wenchuan earthquake, Gorum and Carranza (2015) observed that the coseismic landslides clustered in a narrow band along the strike-slip segment of the fault, while they occurred also much further from the fault along the thrust-slip segment. In particular, most coseismic landslides occurred on the active plate/hanging wall up to 4.7, 8 and 11.5 km from the seismogenic fault in the strike-slip segment, in the oblique-slip segment and in the thrust-slip segment, respectively. According to the dataset published by Dai et al. (2011), a relatively large landslide areal density (> 1%) could be evaluated up to 40 km from the Beichuan-Yinxiu thrust-slip fault segment. For the M_s 7.0 Lushan earthquake, most of the coseismic landslides (landslide area ratio larger than 0.8%) were evaluated in areas with PGA ≥ 0.2 g or within 31 km from the seismogenic fault (Xu et al. 2015). For the Jiuzhaigou earthquake, large landslide areal density (> 0.8%) was observed within just 2 km from the field-inferred seismogenic fault or in areas with PGA ≥ 0.18 g, suggesting that the blind-fault-rupture releases a comparatively smaller energy on the surface. Indeed, also the M_s 7.1 Yushu earthquake, which is another strike-slip earthquake, was characterised by relative large landslide areal density (> 0.12%) within just 4.0 km from the fault (Xu et al. 2013b).

Comparatively, much higher landslide abundance was observed for all the above earthquakes in the active plate/hanging wall side ("hanging wall effect," Xu and Li 2010a). According to the landslide database compiled by Dai et al. (2011), the landslide areal density in the hanging wall was more than double than that in the

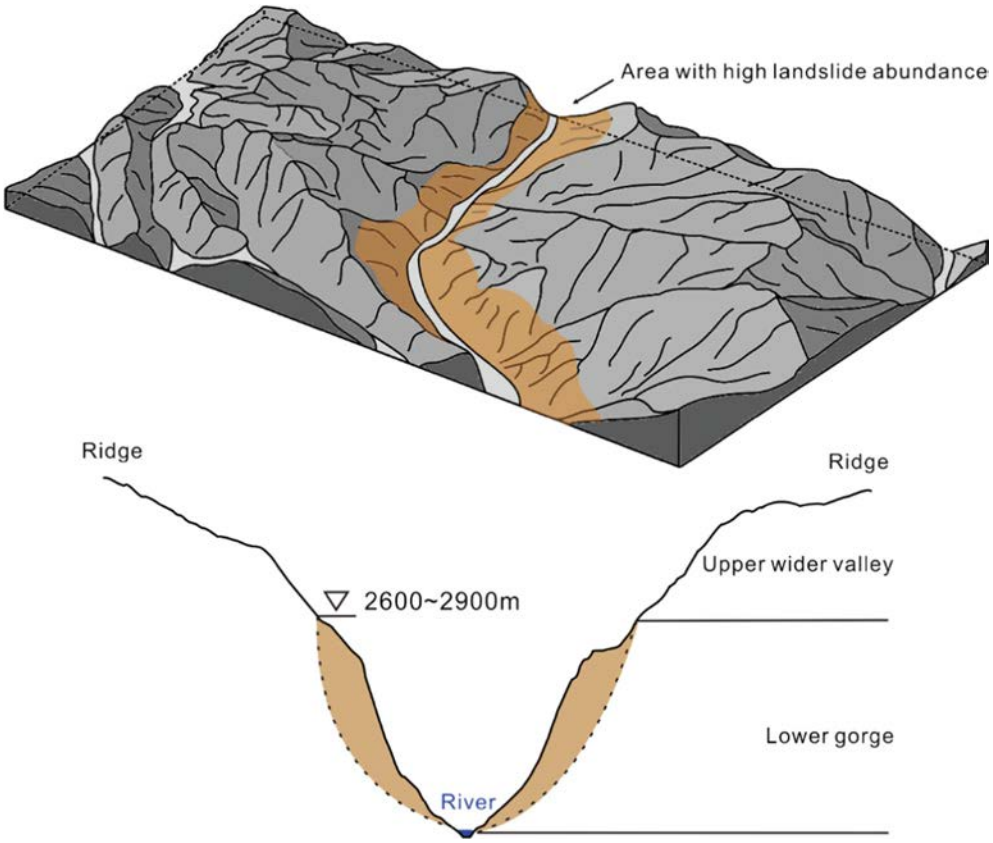

Fig. 10 Micro-landform observed in the study area and its hypothesised effect on landslide occurrence

foot wall for the 2008 Wenchuan earthquake. Moreover, the density dropped below 1% 35 km away from the thrust-slip fault section on the hanging wall, and "just" 15 km away on the foot wall. An even bigger difference can be seen between the active plate and the passive plate for the Jiuzhaigou earthquake strike-slip motion: Fig. 7b (bottom) highlights a landslide areal density twice larger in the NE (active) plate than in the SW (passive) plate.

According to the database by Dai et al. (2011), the landslide areal density increases sharply (> 0.6%) for PGA > 0.40 g for the Wenchuan earthquake. For the Lushan earthquake (Xu et al. 2015), the landslide areal density increases significantly (> 0.2%) for PGA > 0.24 g. For the Jiuzhaigou earthquake (Fig. 8b), the landslide areal density increases significantly (> 0.2%) for PGA > 0.18 g. The lower PGA threshold in this latter case might be due to the local micro-landform, characterised by abundant steep, incised slopes (Fig. 10), which are more easily prone to failure. Conversely, the Lushan epicentral area features gentler river valley terrain.

Regarding the terrain factors, about 53% of the landslides triggered by Wenchuan earthquake occurred within a transition zone with elevation between 1750 and 1950 m and moderately high topographic slope (30–32°) (Gorum et al. 2011). Dai et al. (2011) observed that the landslide areal density peaked between 1000 and 1500 m a.s.l. and increased with the increase of slope angle, especially when it exceeded 35°. The difference between the elevation

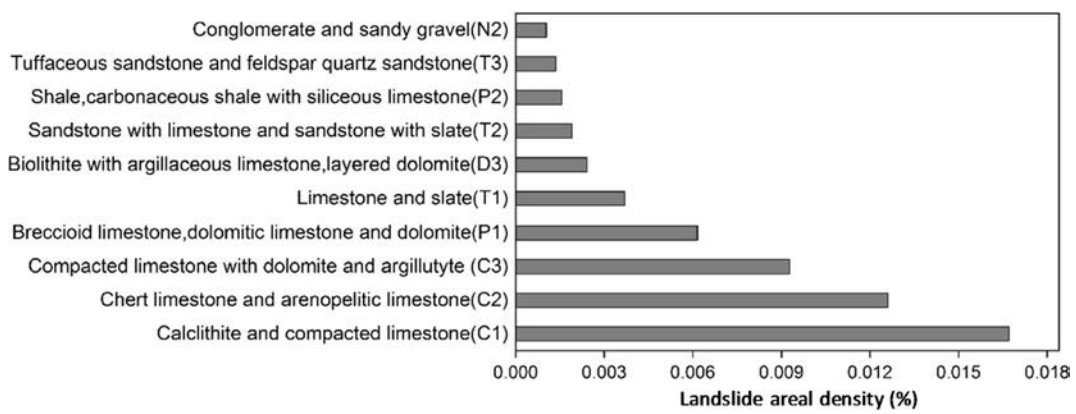

Fig. 11 Relationship between coseismic landslides areal density and lithology

intervals found by the two researches might be due to the different mapping techniques, as Gorum et al. (2011) mapped the landslides by single points representative of the sole source areas. For the Lushan earthquake, Xu et al. (2015) found the highest landslide areal density at elevations ranging from 1000 to 1500 m a.s.l. as well, with the density increasing with the slope angle especially when it exceeded 40°. For the Jiuzhaigou case, the landslide areal density peaks at elevations ranging from 2800 to 3200 m a.s.l. (Fig. 8c) and increases quickly when the slope angle exceeds 40°. The critical slope angle for large landslides abundance (or high landslide areal density) seems correlated with the earthquake magnitude, as both the M_s 7.0 Lushan earthquake and the M_s 7.0 Jiuzhaigou earthquake exhibit a critical angle 5° lower than that evaluated for Wenchuan earthquake.

The influence of the lithology on the landslide occurrence has been controversial for the Wenchuan earthquake: while Dai et al. (2011) suggested that slopes consisting of Pre-Sinian schist or Cambrian sandstone and siltstone intercalated with slate were the most susceptible to failure, Huang and Li (2009) suggested that igneous rocks, carbonatite and sandy conglomerates were the most susceptible, particularly for large-scale landslides. For the Lushan earthquake, Xu et al. (2015) indicated that the largest landslide areal density occurred on slopes composed of igneous rocks or Triassic dolomites. For the Jiuzhaigou earthquake, Carboniferous limestone suffered the largest landslide areal density, followed by the Permian limestone and the Triassic sandstone. Given the limited difference of the tectonic background on the stratum construction and evolution, it seems reasonable to conclude that hard rocks such as igneous rocks, dolomites and limestone are more susceptible to coseismic landslides in the region.

Seismogenic fault identification

The seismogenic fault is usually inferred through the examination of the fault-rupture surface or the fault mechanism solution based on the records from nearby seismometers soon after the earthquake (Keefer 1984). Nevertheless, fault-surface-rupture tracing in the field is a time and resource-consuming work, and for historical earthquake the traces of the coseismic rupture can be obliterated due to both natural and anthropic activities. Obviously, blind-rupture faults are harder to identify as they do not show evident signs on the surface. The use of the fault mechanism solution method requires high-quality seismic wave records, and some uncertainties remain. Aftershocks within 24 h after the main shock can assist to identify seismogenic fault (Kanamori 1977), but it might be difficult to collect enough data of aftershocks if a dense local network of seismometers is not in place (Meunier et al. 2013). Hence, a combination of surface fault-ruptures or mapped fault traces and aftershock recordings (see Fig. 1b) is employed in practice. Furthermore, the spatial distribution of the coseismic landslides can provide a useful insight for identifying the seismogenic fault among possible candidates, both for a recent earthquake and for historical earthquakes since the traces of coseismic landslides are generally preserved better in time than the fault rupture surfaces.

In principle, identifying the seismogenic fault through the coseismic landslides distribution requires all seismic factors that contribute to the landslide distribution to be considered. In practice, an insight can be given by comparing the distribution and the performance of the susceptibility assessment with respect to different hypothesised locations of the seismogenic fault. For thrust-dominated faults, significant landslide clustering was observed on the hanging wall side in historical earthquakes, such as the 1999 M_w 7.6 Chi-Chi earthquake, the 2005 M_w 7.6 Kashmir earthquake, the 2008 M_w 6.9 Iwate-Miyagi Nairiku earthquake and the 2008 M_w 7.9 Wenchuan earthquake (Yagi et al. 2009; Sato et al. 2007; Wang et al. 2003; Huang and Li 2009; Gorum et al. 2011; Huang and Fan 2013; Xu et al. 2013d). Hence, the significant difference in landslide abundance between the two sides of the fault can reasonably help to identify the seismogenic fault. For instance, Meunier et al. (2013) firstly analysed the density pattern of coseismic landslides to track the distribution of fault slip in two large thrust earthquakes in Japan. Xu et al. (2015) identified the blind-thrust seismogenic fault of the M_s 6.6 Lushan earthquake on the basis of changes of landslide density along profiles perpendicular to the strike direction. For strike-slip faults, the difference in landslide abundance across the fault might be limited by the usually sub-vertical fault surface. On the other hand, the horizontal slip component, particularly in the active plate, can be used in combination with the slope aspect for the identification of the orientation of the seismogenic fault. In fact, as shown by Fig. 8g, slopes whose aspect is parallel and discordant with the slip direction are much more susceptible to failure than those whose aspect is parallel and concordant with the slip direction. A similar observation was made by Xu et al. (2013b) for the M_s 7.1 strike-slip Yushu earthquake, which was characterised by similar seismic intensity and fault geometry as the Jiuzhaigou earthquake. Additionally, similar evidence was found in the 2010 M_w 7.2 strike-slip Sierra Cucapah earthquake, which resulted in landslide densities roughly four times higher on slopes with aspect aligned parallel to the horizontal component of the coseismic displacement vector than those that were aligned perpendicular to it (Barlow et al. 2015).

By analysing the controlling factors described in "Spatial distribution patterns of the coseismic landslides and controlling factors" and summarised in Table 2, and assuming the field-inferred fault (Li et al. 2017, Sect. 1) to be the seismogenic fault on the basis of the landslide abundance—slope aspect analysis and "hanging wall" effect (Xu and Li 2010a, Sect. 5.1), a susceptibility map for the coseismic landslides was produced (Fig. S2 in the Online resource 1). A binary logistic regression model was used to conduct the assessment, after normalisation of each factor. The receiver operating characteristic (ROC) curve of the susceptibility assessment was produced, and the area under the curve (AUC) was computed. The AUC of the model resulted equal to 0.851, highlighting a satisfactory prediction precision (see Online resource 1). It is worth noting in Table S2 in Online resource 1 that, besides the slope angle, the slope aspect is the controlling factor which best correlates with the landslide distribution. This is actually well consistent with the earlier considerations on the strong relation between the direction of the strike-slip fault motion (left-lateral motion of the NE plate in the present case) and the slope aspect (Fig. 8g).

Conclusions

In this work, the first comprehensive inventory of the coseismic landslides triggered by the 2017 M_s 7.0 Jiuzhaigou earthquake was presented. The landslides were identified through polygon-based visual interpretation, on the basis of a set of pre- and post-

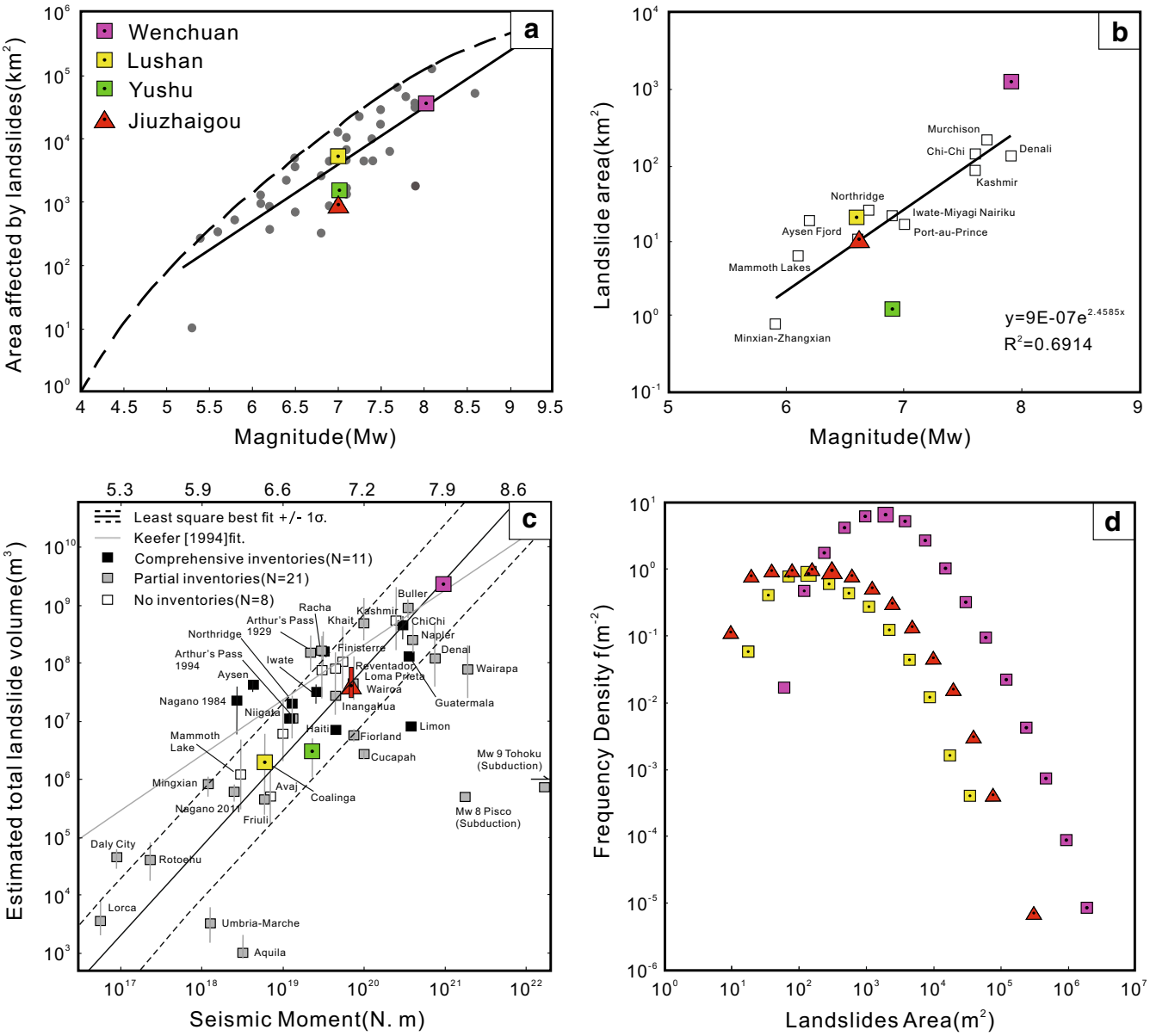

Fig. 12 Jiuzhaigou landslide inventory compared with inventories from other earthquakes. **a** Landslide-affected area and earthquake magnitude (from Keefer 1984, earthquake events occurred before 1980). **b** Total landslide area and earthquake magnitude (from Xu et al. 2015, earthquake events occurred between 1980 and 2013). **c** Estimated total landslide volume and seismic moment (from Marc et al. 2016, data from 40 shallow continental earthquakes; the solid line and dash lines are the empirical prediction and 1σ confidence intervals, respectively, while the grey line is the empirical relationship proposed by Keefer 1994, derived from a smaller database). **d** Landslide area against frequency density relationship for the Jiuzhaigou earthquake, the Lushan earthquake and the Wenchuan earthquake

earthquake high-resolution satellite images and UAV photographs. In total, 1883 landslides were recognised, with a total horizontal projection area of 8.11 km^2 and an estimated total volume in the order of 25–30 × 10^6 m^3.

The landslides occurred mainly along two NE-SW oriented valleys close to the epicentre, within areas with PGA larger than 0.18 g, and consisted mostly of small-scale rock falls and rock/debris slides that developed in proximity of the road and fluvial networks, pointing out a possible important anthropic influence on their occurrence. The critical slope angle, defined as the slope angle at which high landslide abundance occurs, is in the order of 40°, which is consistent with the angle evaluated for the M_s 7.0 Lushan earthquake. Abundance of landslides was also found at elevations around 3000 m a.s.l., where the micro-landform evolves from broad valleys to deep-cut gorges, possibly due to a local ground motion amplification, consistently with what observed for the landslides triggered by the M_s 8.0 Wenchuan earthquake.

The spatial distribution of the coseismic landslides did not correlate sufficiently with the location and orientation of any of the known active faults. On the contrary, the landslides clustered within a distance of just 2 km—in particular on its NE plate (i.e. the fault's active plate)—from a previously unknown blind fault segment characterised by left-lateral strike-slip. The fault location and orientation inferred from the landslides distribution is argued to be the most probable seismogenic fault, which is possibly the

north-western extension of the Huya fault, also dominated by left-lateral strike-slip motion. This finding is consistent with what hypothesised on the basis of field-inferred clues of small surface ruptures and ground displacements.

Acknowledgments

The authors thank the Satellite Environment Center of the Ministry of Environmental Protection and the Sichuan Provincial Surveying and Mapping Geographic Information Bureau for providing high-resolution RS imagery. We thank Dr. Zhengwei He, Dr. Xiujun Dong, Fan Yang, Jing Ren and other students for their supports in collecting the baseline data. We thank Prof. C. Gokceoglu and the three anonymous reviewers for providing us with helpful comments that helped us improve the quality of the manuscript.

Funding information This research is financially supported by the Fund for International Cooperation (NSFC-RCUK_NERC), Resilience to Earthquake-induced landslide risk in China (Grant No. 41661134010), the Funds for Creative Research Groups of China (Grant No. 41521002), National Science Fund for Outstanding Young Scholars of China (Grant No. 41622206), National Science Fund for Distinguished Young Scholars of China (Grant No. 41225011) and AXA fund.

References

Bonini M, Corti G, Delle Donne D et al (2016) Seismic sources and stress transfer interaction among axial normal faults and external thrust fronts in the Northern Apennines (Italy): a working hypothesis based on the 1916–1920 time–space cluster of earthquakes. Tectonophysics 680:67–89. https://doi.org/10.1016/j.tecto.2016.04.045

Barlow J, Barisin I, Rosser N, Petley D, Densmore A, Wright T (2015) Seismically-induced mass movements and volumetric fluxes resulting from the 2010 Mw = 7.2 earthquake in the Sierra Cucapah, Mexico. Geomorphology 230:138–145. https://doi.org/10.1016/j.geomorph.2014.11.012

CENC (2017). China Earthquake Networks Center, China Earthquake Administration. Website: http://www.cenc.ac.cn/. Accessed 11 September 2017.

Chang M, Tang C, Xiao CH et al (2016) Spatial distribution analysis of landslide triggered by the 2013-04-20 Lushan earthquake, China. Earthq Eng Eng Vib 15(1):163–171. https://doi.org/10.1007/s11803-016-0313-5

Chen G, Fan Y, Li Y (2017) Hazard mapping for earthquake-induced geo-disaster chain. In: Hazarika H., Kazama M., Lee W. (eds.) Geotechnical hazards from large earthquakes and heavy rainfalls. Springer, Tokyo, doi: https://doi.org/10.1007/978-4-431-56205-4_33.

Chen SF, Wilson CJL, Deng QD, Zhao XL, Zhi LL (1994) Active faulting and block movement associated with large earthquakes in the min Shan and Longmen mountains, northeastern Tibetan plateau. J Geophys Res Solid Earth 99(B12):24025–24038. https://doi.org/10.1029/94JB02132

Chen XL, Yu L, Wang M, Li JY (2013) Brief communication: landslides triggered by the Ms = 7.0 Lushan earthquake, China. Nature Hazards and Earth System Sciences 1(4):3891–3918. https://doi.org/10.5194/nhessd-1-3891-2013

Chigira M, Yagi H (2006) Geological and geomorphological characteristics of landslides triggered by the 2004 Mid Niigata prefecture earthquake in Japan. Eng Geol 82(4):202–221. https://doi.org/10.1016/j.enggeo.2005.10.006

Chigira M, Wang WN, Furuya T, Kamai T (2003) Geological causes and geomorphological precursors of the Tsaoling landslide triggered by the 1999 Chi-Chi earthquake, Taiwan. Eng Geol 68(3–4):259–273. https://doi.org/10.1016/S0013-7952(02)00232-6

Chigira M, Wu X, Inokuchi T, Wang G (2010) Landslides induced by the 2008 Wenchuan earthquake, Sichuan, China. Geomorphology 118(3-4):225–238. https://doi.org/10.1016/j.geomorph.2010.01.003

Choi JH, Kim YS, Choi SJ (2015) Identification of a suspected quaternary fault in eastern Korea: proposal for a paleoseismic research procedure for the mapping of active faults in Korea. J Asian Earth Sci 113:897–908. https://doi.org/10.1016/j.jseaes.2015.09.014.

Corominas J (1996) The angle of reach as a mobility index for small and large landslides. Can Geotech J 33(2):260–271. https://doi.org/10.1139/t96-005

Croissant T, Lague D, Steer P, Davy P (2017) Rapid post-seismic landslide evacuation boosted by dynamic river width. Nat Geosci 10(9):680–684. https://doi.org/10.1038/ngeo3005

CSI (2017) China Seismic Information Center. China Earthquake Administration, Website http://www.csi.ac.cn/manage/eqDown/05LargeEQ/201708082119M7.0/zonghe.html (Accessed on 11 September 2017

Dai FC, Lee CF (2003) A spatiotemporal probabilistic modelling of storm-induced shallow landsliding using aerial photographs and logistic regression. Earth Surf Process Landforms 28(5):527–545. https://doi.org/10.1002/esp.456

Dai FC, Lee CF, Ngai YY (2002) Landslide risk assessment and management: an overview. Eng Geol 64(1):65–87. https://doi.org/10.1016/S0013-7952(01)00093-X

Dai FC, Xu C, Yao X, Xu L, Tu XB, Gong QM (2011) Spatial distribution of landslides triggered by the 2008 Ms 8.0 Wenchuan earthquake, China. J Asian Earth Sci 40(4):883–895. https://doi.org/10.1016/j.jseaes.2010.04.010

Fan X, Van Westen CJ, Tang C, Xu Q, Huang R, Wang G (2015) The classification of damming landslides and landslide dams induced by the Wenchuan earthquake. Engineering Geology for Society and Territory 2(201):1143–1147. https://doi.org/10.1007/978-3-319-09057-3

Fan X, Van Westen CJ, Korup O, Gorum T, Xu Q, Dai F, Huang R, Wang G (2012) Transient water and sediment storage of the decaying landslide dams induced by the 2008 Wenchuan earthquake, China. Geomorphology 171-172:58–68. https://doi.org/10.1016/j.geomorph.2012.05.003

Fan X, Xu Q, Van Westen CJ, Huang R, Tang R (2017) Characteristics and classification of landslide dams associated with the 2008 Wenchuan earthquake. Geoenvironmental Disasters 4(1):12. https://doi.org/10.1186/s40677-017-0079-8

Gorum T, Fan X, Van Westen CJ, Huang R, Xu Q, Tang C, Wang G (2011) Distribution pattern of earthquake-induced landslides triggered by the 12 May 2008 Wenchuan earthquake. Geomorphology 133(3-4):152–167. https://doi.org/10.1016/j.geomorph.2010.12.030

Gorum T, Van Westen CJ, Korup O, Van Der Meijde M, Fan X, Van Der Meer FD (2013) Complex rupture mechanism and topography control symmetry of mass-wasting pattern, 2010 Haiti earthquake. Geomorphology 184:127–138. https://doi.org/10.1016/j.geomorph.2012.11.027

Gorum T, Carranza EJM (2015) Control of style-of-faulting on spatial pattern of earthquake-triggered landslides. Int J Environ Sci Technol 12(10):3189–3212. https://doi.org/10.1007/s13762-015-0752-y

Guzzetti F, Ardizzone F, Cardinali M, Rossi M, Valigi D (2009) Landslide volumes and landslide mobilization rates in Umbria, central Italy. Earth Planet Sci Lett 279(3-4):222–229. https://doi.org/10.1016/j.epsl.2009.01.005

Has B, Nozaki T (2014) Role of geological structure in the occurrence of earthquake-induced landslides, the case of the 2007 Mid-Niigata Offshore earthquake, Japan. Eng Geol 182(A:25–36. https://doi.org/10.1016/j.enggeo.2014.09.006

Hartvich F, Valenta J (2013) Tracing an intra-montane fault: an interdisciplinary approach. Surv Geophys 34(3):317–347. https://doi.org/10.1007/s10712-012-9216-9

Huang MH, Fielding EJ, Liang C, Milillo P, Bekaert D, Dreger D, Salzer J (2017) Coseismic deformation and triggered landslides of the 2016 Mw 6.2 Amatrice earthquake in Italy. Geophys Res Lett 44(3):1266–1274. https://doi.org/10.1002/2016GL071687

Huang R, Fan X (2013) The landslide story. Nat Geosci 6(5):325–326. https://doi.org/10.1038/ngeo180.

Huang R, Li WL (2008) Research on development and distribution rules of geohazards induced by Wenchuan earthquake induced by Wenchuan earthquake on 12th May, 2008. Chin J Rock Mech Eng 27(12):2585–2592

Huang R, Li WL (2009) Analysis of the geo-hazards triggered by the 12 May 2008 Wenchuan earthquake, China. Bull Eng Geol Environ 68(3):363–371. https://doi.org/10.1007/s10064-009-0207-0

Huang R, Pei X, Fan X, Zhang F, Li S, Li B (2012) The characteristics and failure mechanism of the largest landslide triggered by the Wenchuan earthquake, May 12, 2008, China. Landslides 9(1):131–142. https://doi.org/10.1007/s10346-011-0276-6

Hungr O, Leroueil S, Picarelli L (2014) The Varnes classification of landslide types, an update. Landslides 11(2):167–194. https://doi.org/10.1007/s10346-013-0436-y

Kanamori H (1977) The energy release in great earthquakes. J Geophys Res 82(20):2981–2987. https://doi.org/10.1029/JB082i020p02981

Kargel JS, Leonard GJ, Shugar DH et al (2016) Geomorphic and geologic controls of geohazards induced by Nepal's 2015 Gorkha earthquake. Science 351(6269):aac8353. https://doi.org/10.1126/science.aac8353

Keefer DK (1984) Landslides caused by earthquakes. Geol Soc Am Bull 95(4):406–421. https://doi.org/10.1130/0016-7606(1984)95<406:LCBE>2.0.CO;2

Keefer DK (1994) The importance of earthquake-induced landslides to long-term slope erosion and slope-failure hazards in seismically active regions. Geomorphology 10(1-4):265–284. https://doi.org/10.1016/0169-555X(94)90021-3

Keefer DK (2000) Statistical analysis of an earthquake-induced landslide distribution—the 1989 Loma Prieta, California event. Eng Geol 58(3):231–249. https://doi.org/10.1016/S0013-7952(00)00037-5

Keefer DK (2002) Investigating landslides caused by earthquakes—a historical review. Surv Geophys 23(6):473–510. https://doi.org/10.1023/A:102127471.

Keefer DK (2010) Earthquake-induced landslides from horseback surveys through GIS analyses (Sergey Soloviev Medal Lecture). Geophysical Research Abstracts 12:EGU2010-14677 EGU General Assembly

Larsen IJ, Montgomery DR, Korup O (2010) Landslide erosion controlled by hillslope material. Nat Geosci 3(4):247–251. https://doi.org/10.1038/ngeo776

Le Béon M, Huang MH, Suppe J et al (2017) Shallow geological structures triggered during the Mw 6.4 Meinong earthquake, southwestern Taiwan. Terr Atmos Ocean Sci 28(5):663–681. https://doi.org/10.3319/TAO.2017.03.20.02

Li Y, Huang C, Yi S, Wu C (2017) Study on seismic fault and source rupture tectonic dynamic mechanism of Jiuzhaigou Ms 7.0 earthquake. Journal of Engineering Geology (in Chinese) 25(4):1141–1150

Li C, Xu W, Wu J, Gao M (2016a) Using new models to assess probabilistic seismic hazard of the north–south seismic zone in China. Nat Hazards 82(1):659–681. https://doi.org/10.1007/s11069-016-2212-5

Li G, West AJ, Densmore AL, Hammond DE, Jin Z, Zhang F, Wang J, Hilton RG (2016b) Connectivity of earthquake-triggered landslides with the fluvial network: implications for landslide sediment transport after the 2008 Wenchuan earthquake. Journal of Geophysical Research: Earth Surface 121(4):703–724. https://doi.org/10.1002/2015JF003718

Lu J, Shen Z, Wang M (2003) Contemporary crustal deformation and active tectonic block model of the Sichuan-Yunnan region, China. Seismol Geol (in Chinese) 25(4):543–554

Malamud BD, Turcotte DL, Guzzetti F, Reichenbach P (2004) Landslide inventories and their statistical properties. Earth Surf. Process. Landforms 29(6):687–711. https://doi.org/10.1002/esp.1064

Marc O, Hovius N, Meunier P, Gorum T, Uchida T (2016) A seismologically consistent expression for the total area and volume of earthquake-triggered landsliding. J Geophys Res Earth Surf 121(4):640–663. https://doi.org/10.1002/2015JF003732

Mathew J, Jha VK, Rawat GS (2009) Landslide susceptibility zonation mapping and its validation in part of Garhwal Lesser Himalaya, India, using binary logistic regression analysis and receiver operating characteristic curve method. Landslides 6(1):17–26. https://doi.org/10.1007/s10346-008-0138-z

Menard S (2002) Applied logistic regression analysis, vol. 106. Sage. https://doi.org/10.4135/9781412983433

Meunier P, Hovius N, Haines AJ (2007) Regional patterns of earthquake-triggered landslides and their relation to ground motion. Geophys Res Lett 34(20):L20408. https://doi.org/10.1029/2007GL031337

Meunier P, Uchida T, Hovius N (2013) Landslide patterns reveal the sources of large earthquakes. Earth Planet Sc Lett 363:27–33. https://doi.org/10.1016/j.epsl.2012.12.018

Odin M, Meunier P, Hovius N (2017) Prediction of the area affected by earthquake-induced landsliding based on seismological parameters. Nat Hazards Earth Syst Sci 17(7):1159–1175. https://doi.org/10.5194/nhess-17-1159-2017

Parker RN, Densmore AL, Rosser NJ, De Michele M, Yong L, Huang R, Whadcoat S, Petley DN (2011) Mass wasting triggered by the 2008 Wenchuan earthquake is greater than orogenic growth. Nat Geosci 4(7):449–452. https://doi.org/10.1038/ngeo1154

Qi S, Xu Q, Lan H, Zhang B, Liu J (2010) Spatial distribution analysis of landslides triggered by 2008.5.12 Wenchuan earthquake, China. Eng Geol 116(1-2):95–108. https://doi.org/10.1016/j.enggeo.2010.07.011

Ren J, Xu X, Zhang S, Yeats RS, Chen J, Zhu A, Liu S (2017) Surface rupture of the 1933 M 7.5 Diexi earthquake in eastern Tibet: implications for seismogenic tectonics. Geophys J Int 212(3):1627–1644. https://doi.org/10.1093/gji/ggx498

Ren XM, Zhao WM, Chai CZ et al (2002) Estimation of recurrent interval of strong earthquakes in NS earthquake belt. Inland Earthq 16(1):69–75 **(in Chinese)**

Roback K, Clark MK, West AJ et al (2017) The size, distribution, and mobility of landslides caused by the 2015 Mw7.8 Gorkha earthquake. Nepal Geomorphology. https://doi.org/10.1016/j.geomorph.2017.01.030

Robinson TR, Rosser NJ, Densmore AL, Williams JG, Kincey ME, Benjamin J, Bell HJA (2017) Rapid post-earthquake modelling of coseismic landslide magnitude and distribution for emergency response decision support. Nat Hazards Earth Syst Sci:1–29. https://doi.org/10.5194/nhess-2017-83

Sato HP, Hasegawa H, Fujiwara S, Tobita M, Koarai M, Une H, Iwahashi J (2007) Interpretation of landslide distribution triggered by the 2005 Northern Pakistan earthquake using SPOT 5 imagery. Landslides 4(2):113–122. https://doi.org/10.1007/s10346-006-0069-5

Schumacher M, Roßner R, Vach W (1996) Neural networks and logistic regression: part I. Computational Statistics & Data Analysis 21(6):661–682. https://doi.org/10.1016/0167-9473(95)00032-1

Sekiguchi H, Irikura K, Iwata T (2000) Fault geometry at the rupture termination of the 1995 Hyogo-ken Nanbu earthquake. Bull Seismol Soc Am 90(1):117–133. https://doi.org/10.1785/0119990027

Semmane F, Cotton F, Campillo M (2005) The 2000 Tottori earthquake: a shallow earthquake with no surface rupture and slip properties controlled by depth. J Geophys Res 110(B3):B03306. https://doi.org/10.1029/2004JB003194

Shen ZK, Lü JN, Wang M et al (2005) Contemporary crustal deformation around the southeast borderland of the Tibetan Plateau. J Geophys Res 2005(B11):110 (B11409). https://doi.org/10.1029/2004JB003421

Tang C, Ma G, Chang M, Li W, Zhang D, Jia T, Zhou Z (2015) Landslides triggered by the 20 April 2013 Lushan earthquake, Sichuan Province, China. Eng Geol 187:45–55. https://doi.org/10.1016/j.enggeo.2014.12.004

Tanoli JI, Ningsheng C, Regmi AD, Jun L (2017) Spatial distribution analysis and susceptibility mapping of landslides triggered before and after Mw7.8 Gorkha earthquake along upper Bhote Koshi, Nepal. Arab J Geosci 10(13). https://doi.org/10.1007/s12517-017-3026-9

UNESCO (1992). World heritage nomination—advisory body evaluation (IUCN). 637: Jiuzhaigou Valley scenic and historic interest area (China). Website: http://whc.unesco.org/document/153932. Accessed 14 October 2017.

USGS (2017). United States geological survey. Earthquake Hazards Program. Website: https://earthquake.usgs.gov/earthquakes/eventpage/us2000a5x1#executive. Accessed 11 September 2017.

Wang G, Huang R, Lourenço DN, Kamai T (2014) A large landslide triggered by the 2008Wenchuan (M8.0) earthquake in Donghekou area: phenomena and mechanisms. Eng Geol 182:148–157. https://doi.org/10.1016/j.enggeo.2014.07.013.

Wang WN, Wu HL, Nakamura H, Wu SC, Ouyang S, Yu MF (2003) Mass movements caused by recent tectonic activity: the 1999 Chi-Chi earthquake in central Taiwan. Island Arc 12(4):325–334. https://doi.org/10.1046/j.1440-1738.2003.00400.x

Wei M, Sandwell D, Fialko Y, Bilham R (2011) Slip on faults in the Imperial Valley triggered by the 4 April 2010 Mw 7.2 El Mayor-Cucapah earthquake revealed by InSAR. Geophys Res Lett 38(1):L01308. https://doi.org/10.1029/2010GL045235

Xiaoli C, Qing Z, Chunguo L (2015) Distribution pattern of coseismic landslides triggered by the 2014 Ludian, Yunnan, China Mw6.1 earthquake: special controlling conditions of local topography. Landslides 12(6):1159–1168. https://doi.org/10.1007/s10346-015-0641-y

Xu C, Xu X (2013) Response rate of seismic slope mass movements related to 2008 Wenchuan earthquake and its spatial distribution analysis. J Eng Geol S2:3888–3908

Xu C, Xu X (2014) The spatial distribution pattern of landslides triggered by the 20 April 2013 Lushan earthquake of China and its implication to identification of the seismogenic fault. Chin Sci Bull 59(13):1416–1424. https://doi.org/10.1007/s11434-014-0202-0

Xu C, Xu X, Wu XY et al (2013a) Detailed inventories of landslide triggered by 2008 Wenchuan earthquake and their spatial distribution statistical analyses. J Eng Geol 21(1):25–44

Xu C, Xu X, Yu G (2013b) Landslides triggered by slipping-fault-generated earthquake on a plateau: an example of the 14 April 2010, Ms 7.1, Yushu, China earthquake. Landslides 10(4):421–431. https://doi.org/10.1007/s10346-012-0340-x

Xu C, Xu XW, Zheng WJ (2013c) Compiling inventory of landslides triggered by Minxian-Zhangxian earthquake of July 22, 2013 and their spatial distribution analysis. Journal of Engineering Geology 21(5):736–749

Xu C, Xu X, Zhou B, Yu G (2013d) Revisions of the M 8.0 Wenchuan earthquake seismic intensity map based on co-seismic landslide abundance. Nat Hazards 69(3):1459–1476. https://doi.org/10.1007/s11069-013-0757-0

Xu C, Shyu JBH, Xu X (2014) Landslides triggered by the 12 January 2010 Port-au-Prince, Haiti, Mw = 7.0 earthquake: visual interpretation, inventory compiling, and spatial distribution statistical analysis. Nat Hazards Earth Syst Sci 14(7):1789–1818. https://doi.org/10.5194/nhess-14-1789-2014

Xu C, Xu X, Shyu JBH (2015) Database and spatial distribution of landslides triggered by the Lushan, China Mw 6.6 earthquake of 20 April 2013. Geomorphology 248:77–92. https://doi.org/10.1016/j.geomorph.2015.07.002

Xu C, Xu X, Shen L, Yao Q, Tan X, Kang W, Ma S, Wu X, Cai J, Gao M, Li K (2016) Optimized volume models of earthquake-triggered landslides. Sci Rep 6(1). https://doi.org/10.1038/srep29797
Xu Q, Li WL (2010a) Study on the direction effects of landslides triggered by Wenchuan earthquake. Journal of Sichuan University (Engineering Science Edition) S1:7–14
Xu Q, Li WL (2010b) Distribution of large-scale landslides induced by the Wenchuan earthquake. J Eng Geol 18(6)
Xu X, Wen X, Chen G, Yu G (2008) Discovery of the Longriba fault zone in eastern Bayan Har block, China and its tectonic implication. Sci China Ser D Earth Sci 51(9):1209–1223. https://doi.org/10.1007/s11430-008-0097-1
Xu X, Wen X, Yu G, Chen G, Klinger Y, Hubbard J, Shaw J (2009) Coseismic reverse- and oblique-slip surface faulting generated by the 2008 Mw 7.9 Wenchuan earthquake, China. Geology 37(6):515–518. https://doi.org/10.1130/G25462A.1
Yagi H, Sato G, Higaki D, Yamamoto M, Yamasaki T (2009) Distribution and characteristics of landslides induced by the Iwate–Miyagi Nairiku earthquake in 2008 in Tohoku District, Northeast Japan. Landslides 6(4):335–344. https://doi.org/10.1007/s10346-009-0182-3
Yin A, Harrison TM (2000) Geologic evolution of the Himalayan-Tibetan orogen. Annu Rev Earth Planet Sci 28(1):211–280. https://doi.org/10.1146/annurev.earth.28.1.211
Zhang S, Zhang LM (2017) Impact of the 2008 Wenchuan earthquake in China on subsequent long-term debris flow activities in the epicentral area. Geomorphology 276:86–103. https://doi.org/10.1016/j.geomorph.2016.10.009
Zhou R, Li Y, Alexander LD et al (2006) Active tectonics of the eastern margin of the Tibet plateau. J Miner Petrol (in Chinese) 26(2):40–51
Zhou S, Chen G, Fang L (2016) Distribution pattern of landslides triggered by the 2014 Ludian earthquake of China: implications for regional threshold topography and the Seismogenic fault identification. ISPRS Int J Geo-Inf 5(4):46. https://doi.org/10.3390/ijgi5040046

Electronic supplementary material The online version of this article (https://doi.org/10.1007/s10346-018-0960-x) contains supplementary material, which is available to authorized users.

X. Fan (✉) · G. Scaringi · Q. Xu (✉) · W. Zhan · L. Dai · Y. Li · X. Pei · Q. Yang · R. Huang
The State Key Laboratory of Geohazards Prevention and Geoenvironment Protection (SKLGP),
Chengdu University of Technology,
Chengdu, Sichuan 610059, China
Email: fxm_cdut@qq.com
Email: xuqiang_68@126.com

W. Zhan
Glenn Department of Civil Engineering,
Clemson University,
Clemson, SC 29634, USA